Electronic Supplementary Information

For the Manuscript Entitled

Cobalt complexes of pyrrolecarboxamide ligands as catalysts in nitro reduction reactions: Influence of electronic substituents on catalysis and mechanistic insights

Sunil Yadav, Sushil Kumar and Rajeev Gupta*

Department of Chemistry, University of Delhi, Delhi – 110 007

Index

List of Figures:

List of Tables:

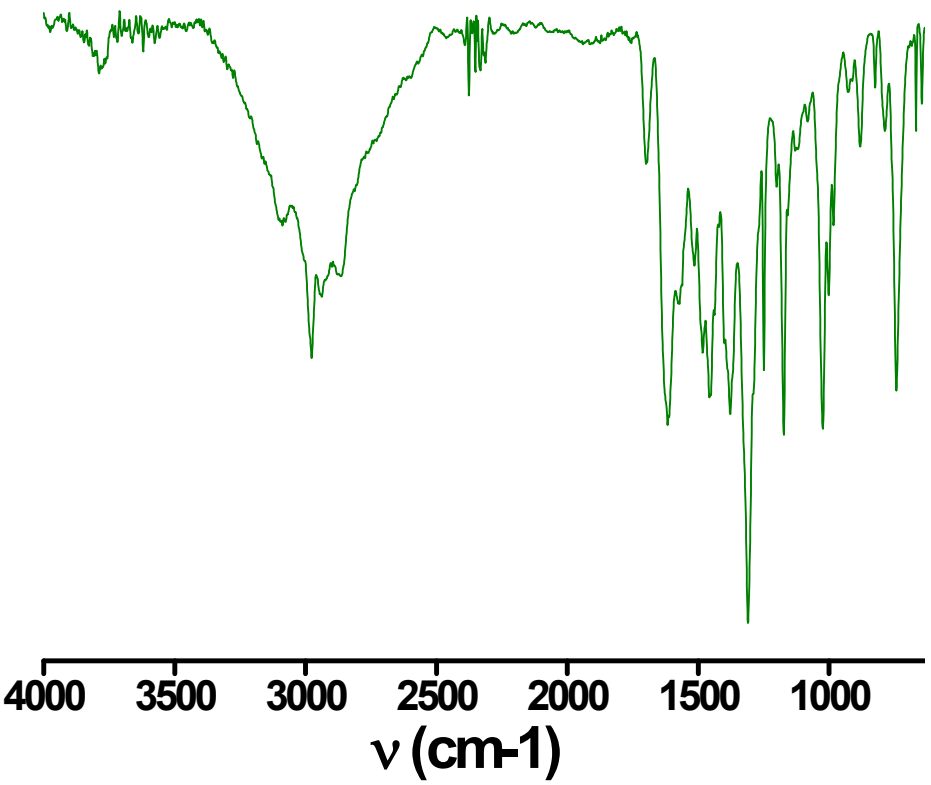

Figure S1. FTIR spectrum of complex **1**.

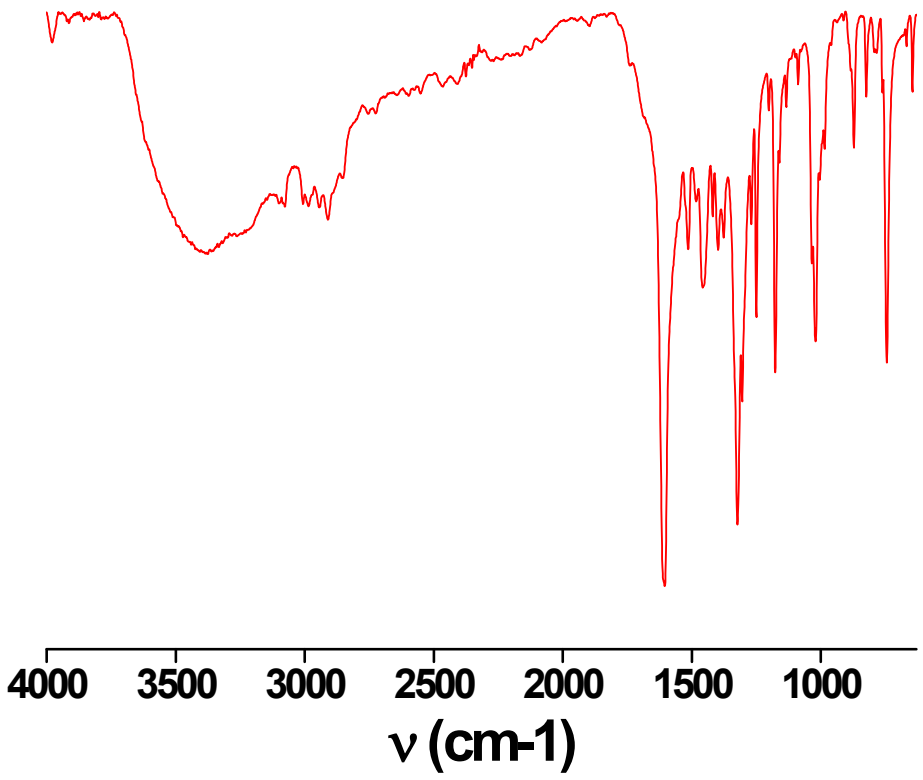

Figure S2. FTIR spectrum of complex **2**.

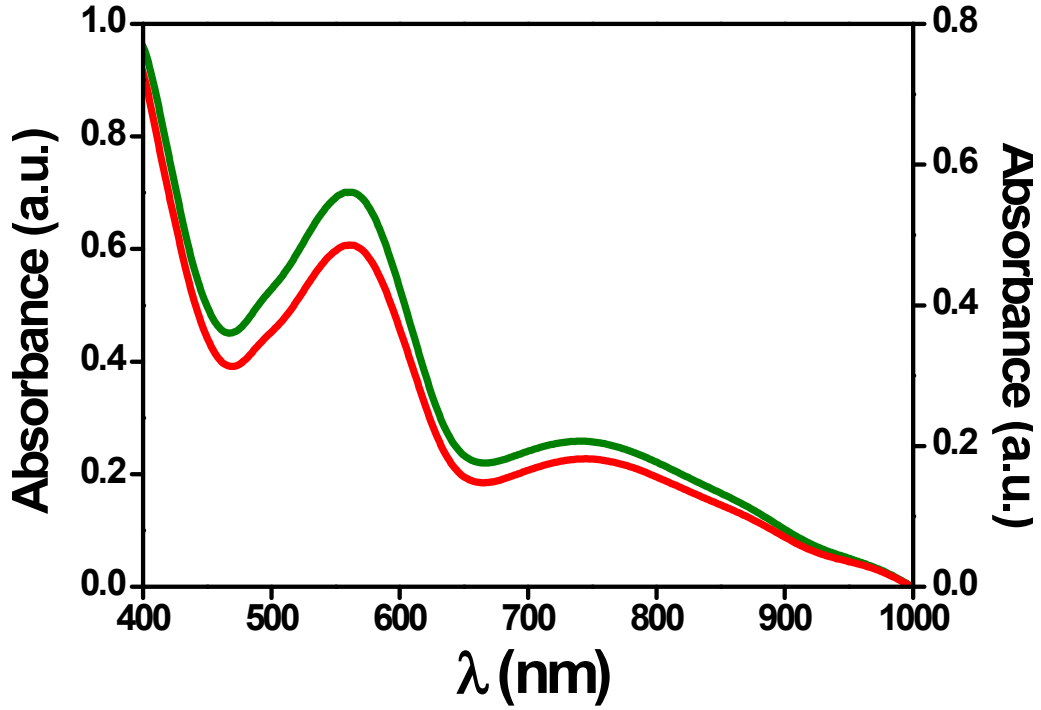

Figure S3. UV/Vis spectra of complex **1** (green trace) and **2** (red trace) measured in MeOH.

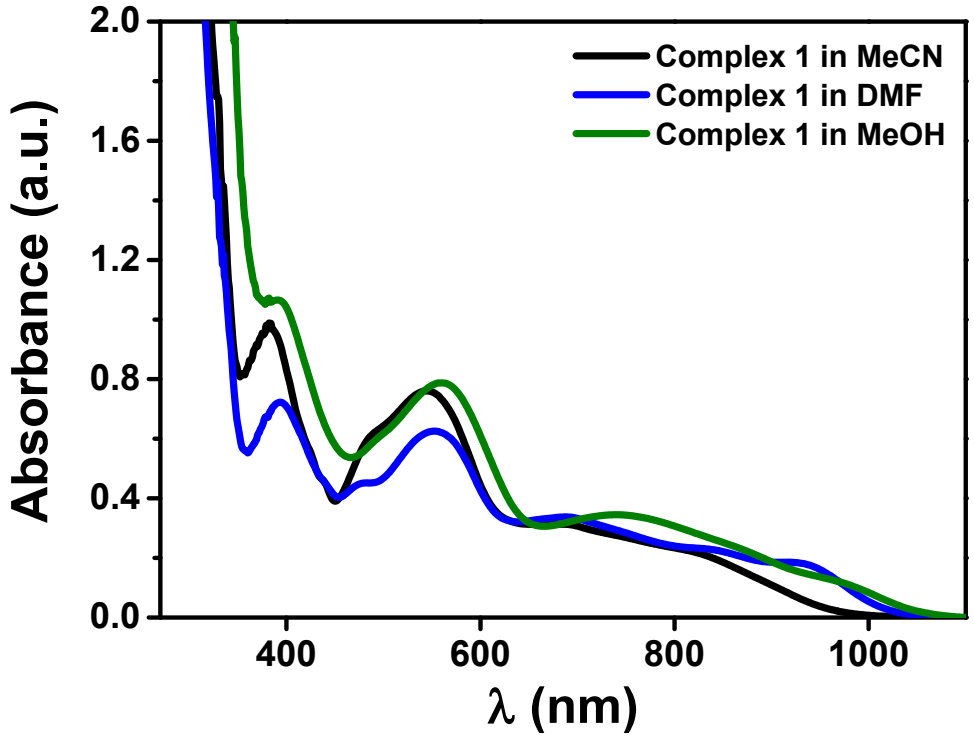

Figure S4. Comparative UV/Vis spectra of complex **1** in MeCN (black trace), DMF (blue trace), and MeOH (green trace).

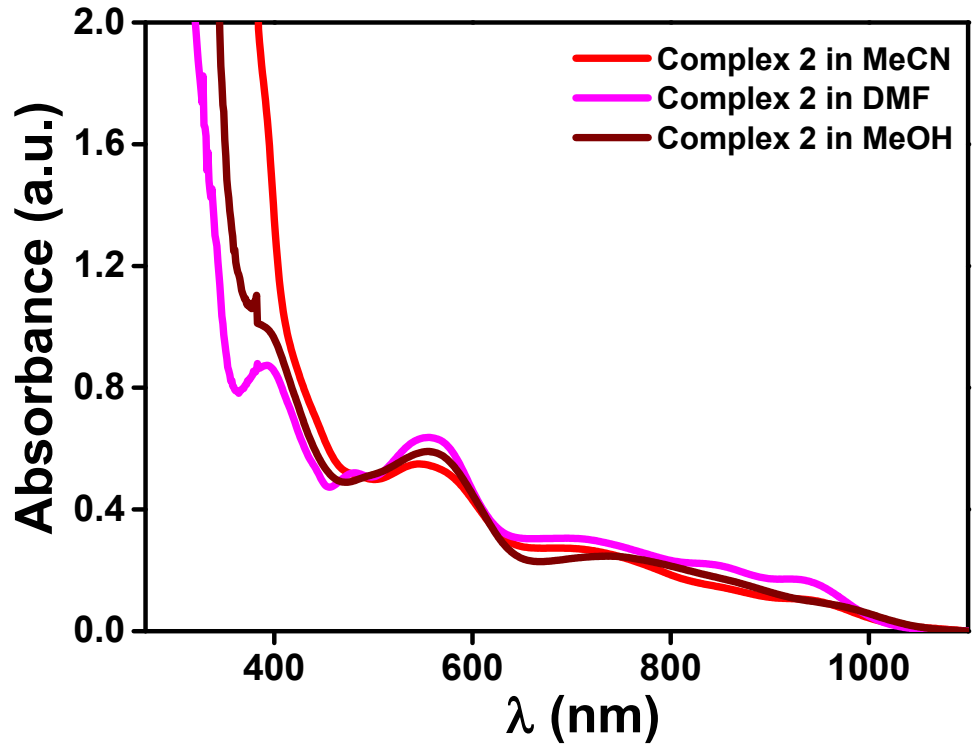

Figure S5. Comparative UV/Vis spectra of complex **2** in MeCN (red trace), DMF (pink trace), and MeOH (brown trace).

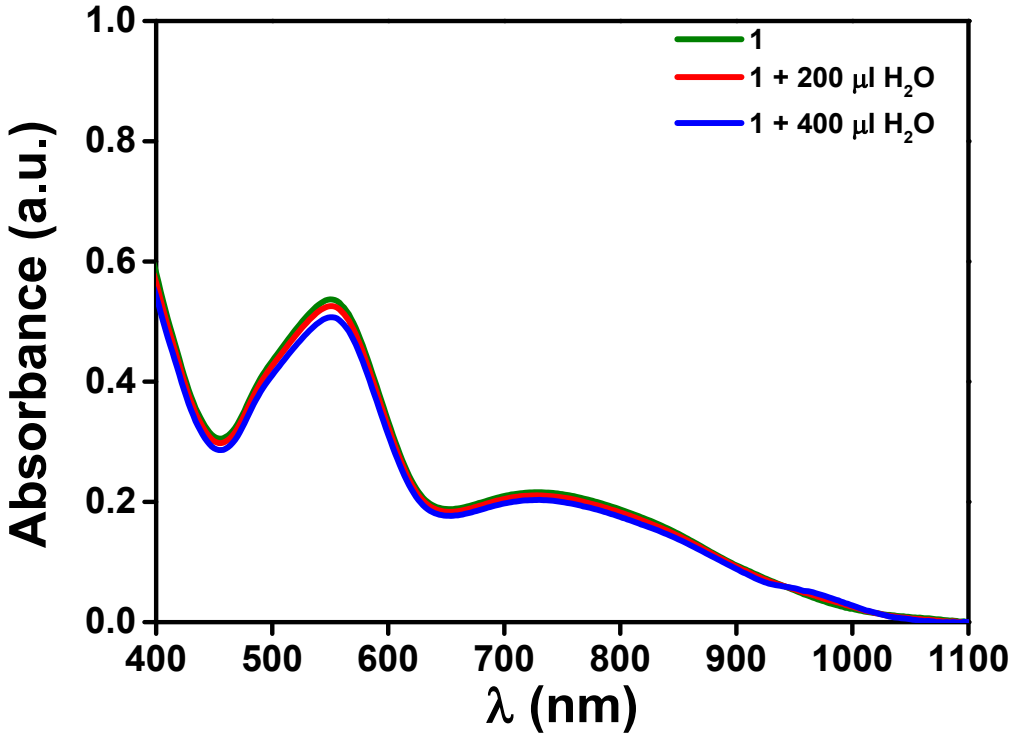

Figure S6. UV/Vis spectrum of complex **1** recorded in MeOH (green trace) and after addition of H_2O (red and blue traces).

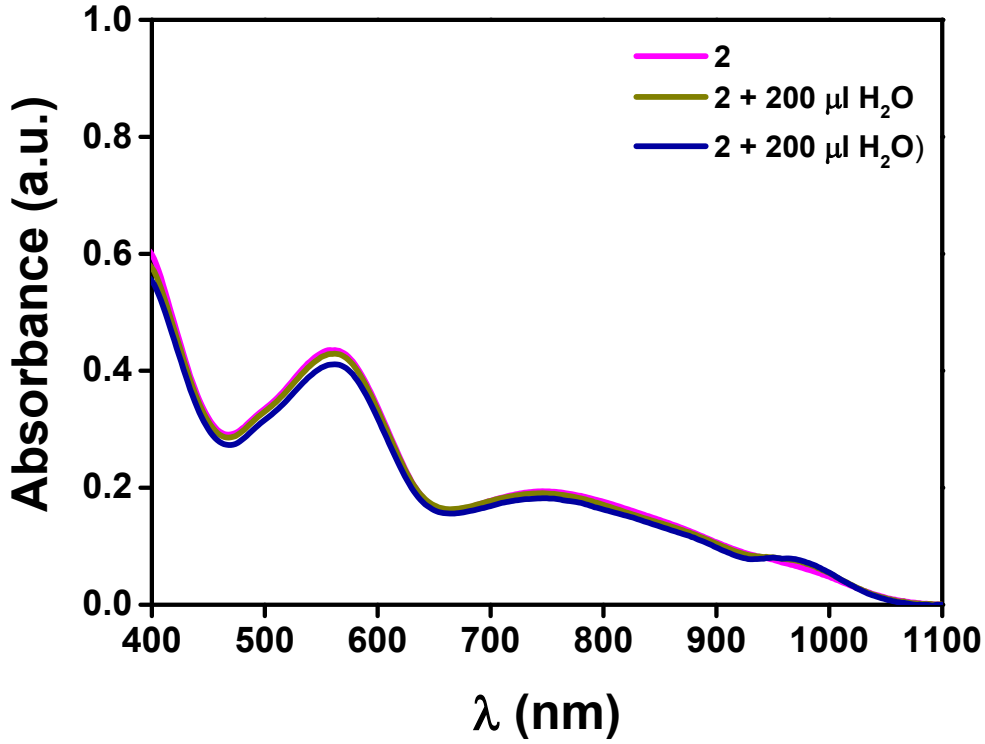

Figure S7. UV/Vis spectrum of complex **2** recorded in MeOH (pink trace) and after addition of H_2O (green and dark blue traces).

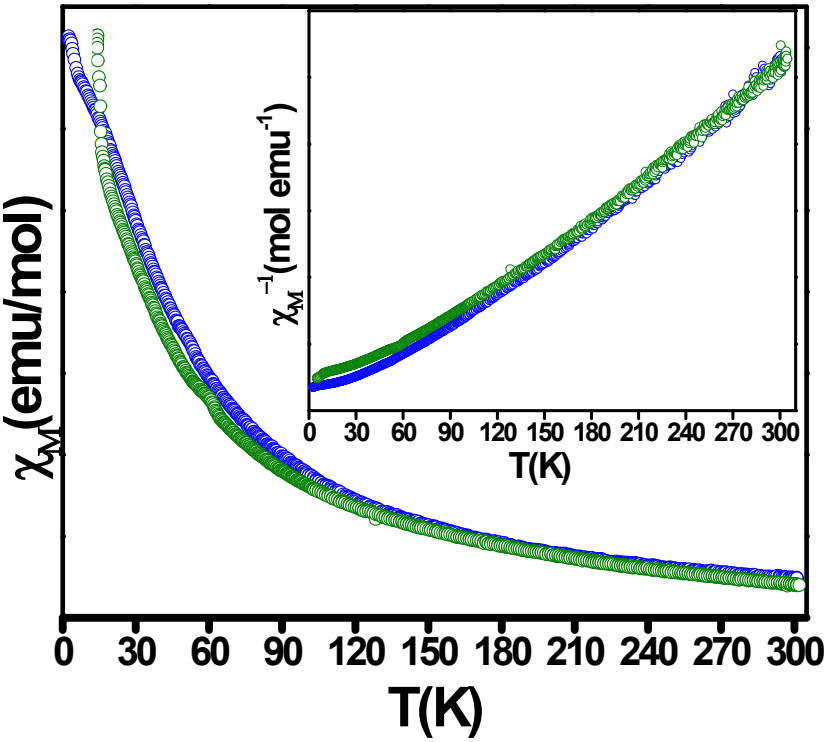

Figure S8. Plots of molar susceptibility (χ_M) and inverse molar susceptibility (χ_M^{-1}) versus temperature for complex **1** (blue circles) and **2** (green circles) measured at 0.5 T.

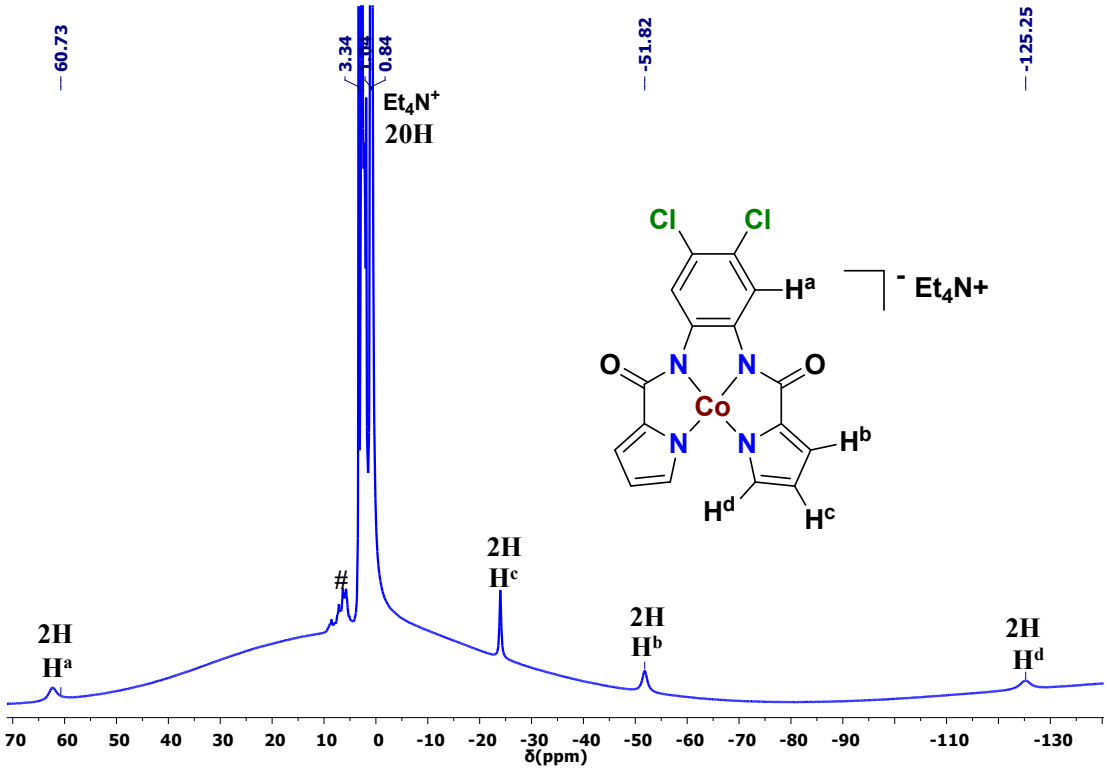

Figure S9. ^{1}H NMR spectrum of complex **1** recorded in CD_3CN. * and # respectively represent the residual solvent peak and some unidentified impurity.

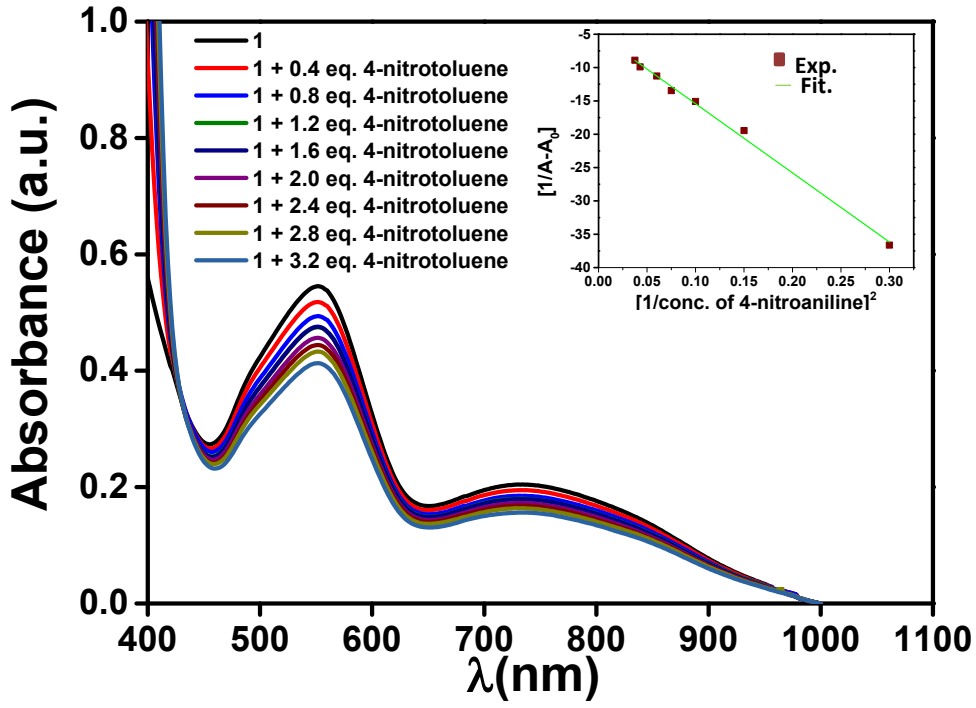

Figure. S10. UV-Vis titration of complex **1** with 4-nitrotolene in MeOH. Top Inset: Change in absorbance as a function of moles of 4-nitrotolene. Bottom Inset: Linear regression fitting curve for 1:2 binding between complex **1** and 4-nitrotolene.

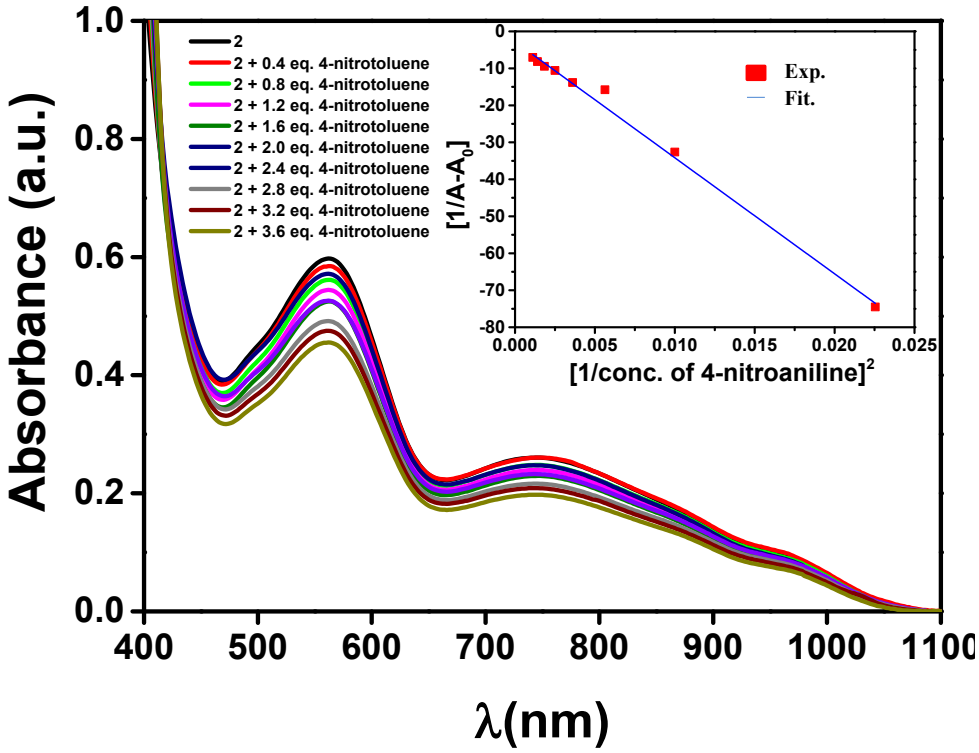

Figure. S11. UV-Vis titration of complex **2** with 4-nitrotolene in MeOH. Top Inset: Change in absorbance as a function of moles of 4-nitrotolene. Bottom Inset: Linear regression fitting curve for 1:2 binding between complex **2** and 4-nitrotolene.

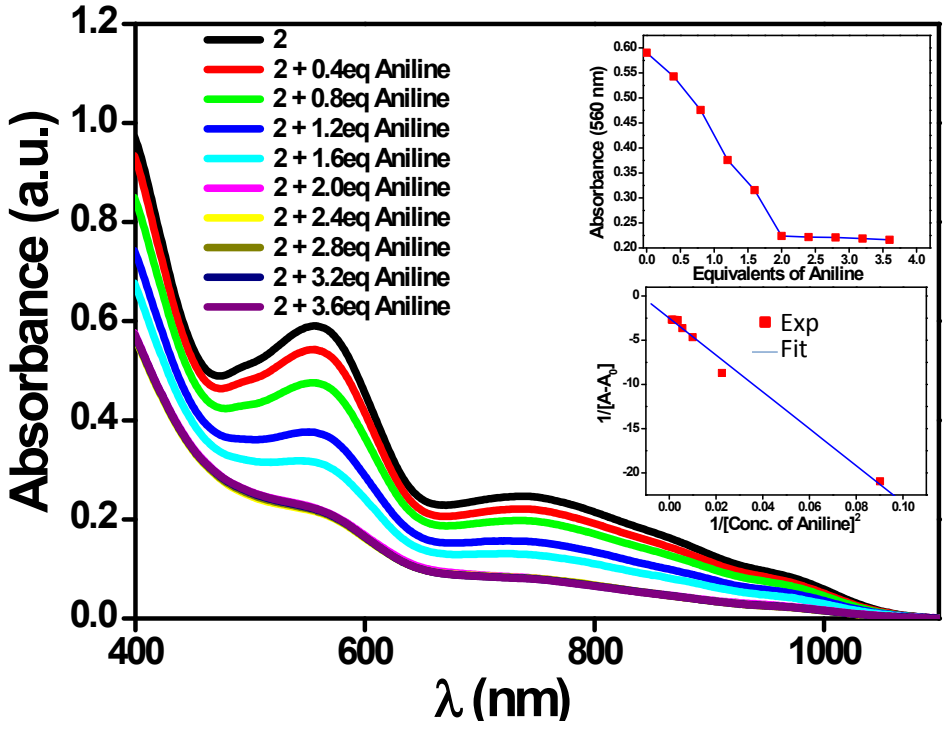

Figure. S12. UV-Vis titration of complex **2** with aniline in MeOH. Top Inset: Change in absorbance as a function of moles of aniline. Bottom Inset: Linear regression fitting curve for 1:2 binding between complex **2** and aniline.

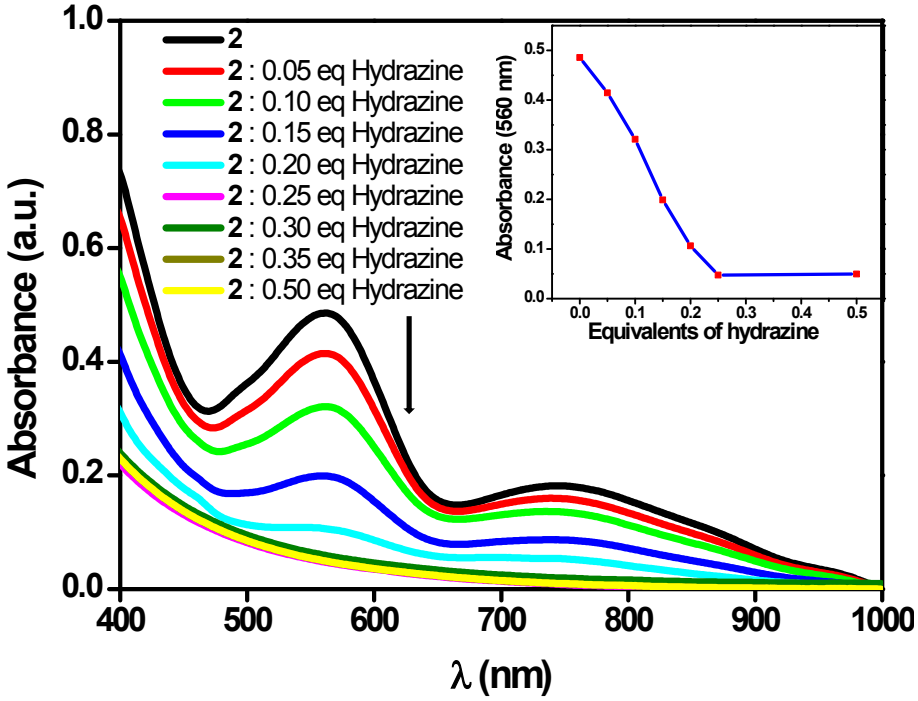

Figure S13. UV-Vis spectral titration of complex **2** with hydrazine in MeOH; and change in absorption intensity as a function of moles of hydrazine (inset).

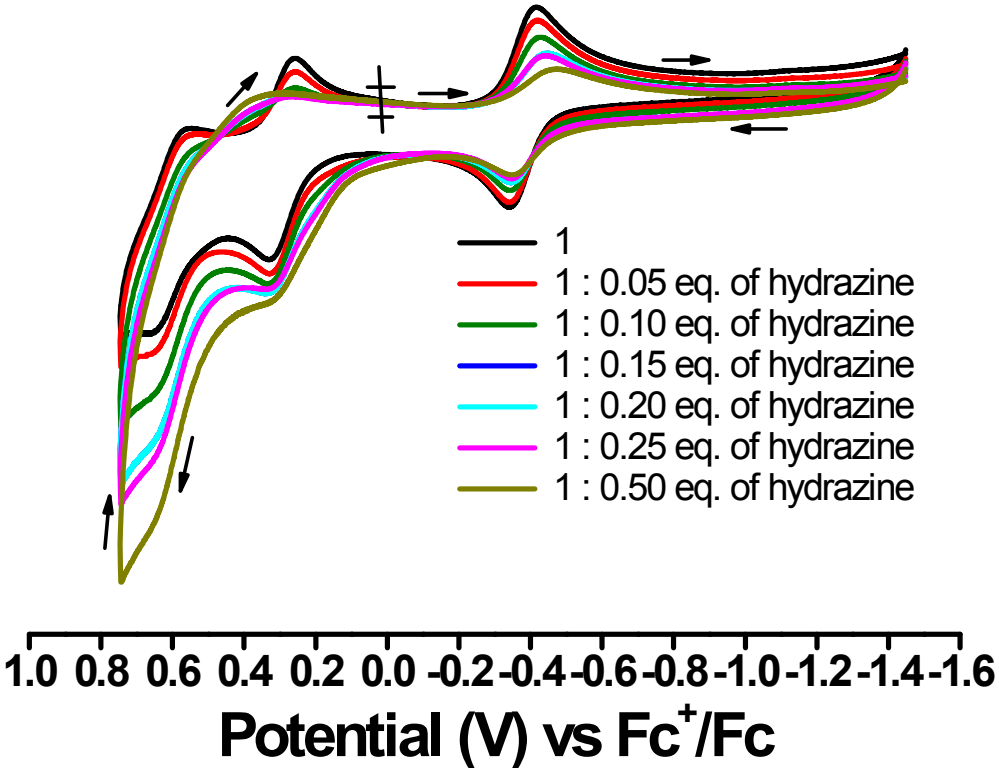

Figure S14. Change in cyclic voltammograms of complex **1** as a function of hydrazine in MeOH.

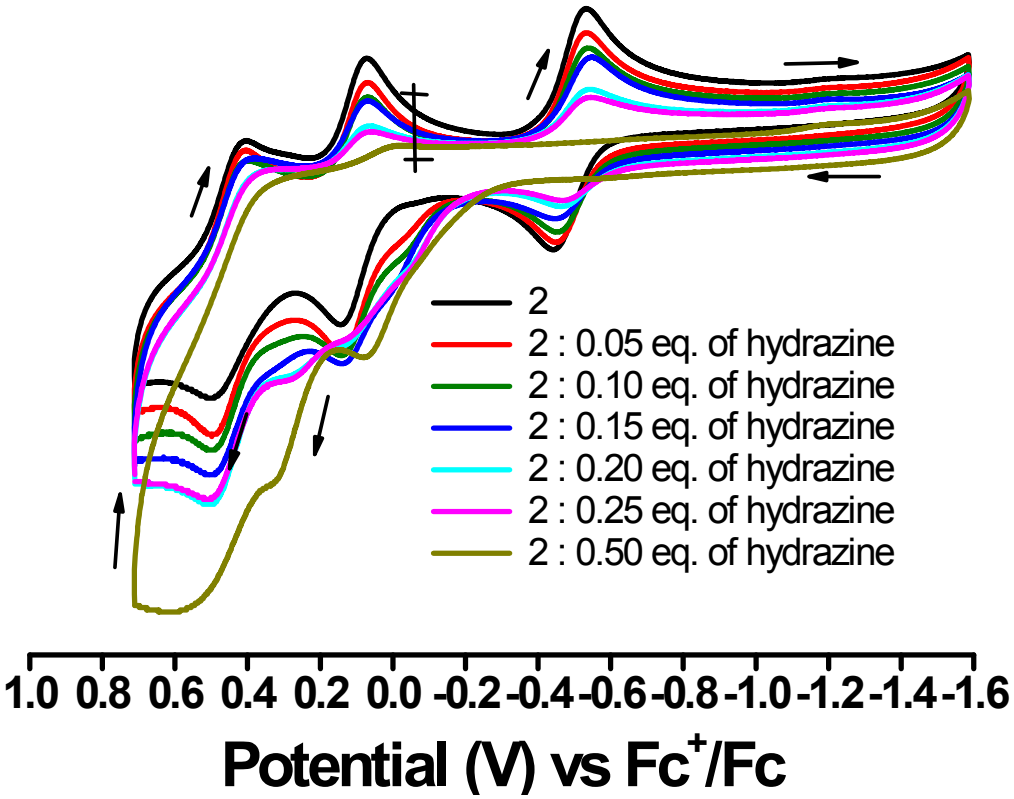

Figure S15. Change in cyclic voltammograms of complex **2** as a function of hydrazine in MeOH.

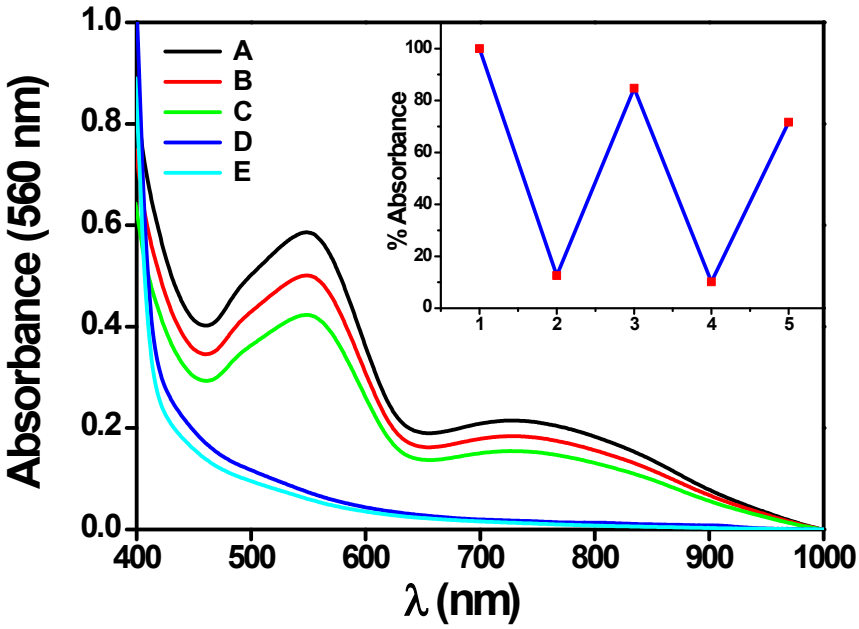

Figure S16. Recyclability experiment of complex **2** with respect to hydrazine; original absorption spectrum of complex **2** (trace A) followed by reduction with 0.25 equiv. NH_2NH_2 further followed by oxidation with O_2 (traces B – E). Inset displays subsequent two regenerative cycles.

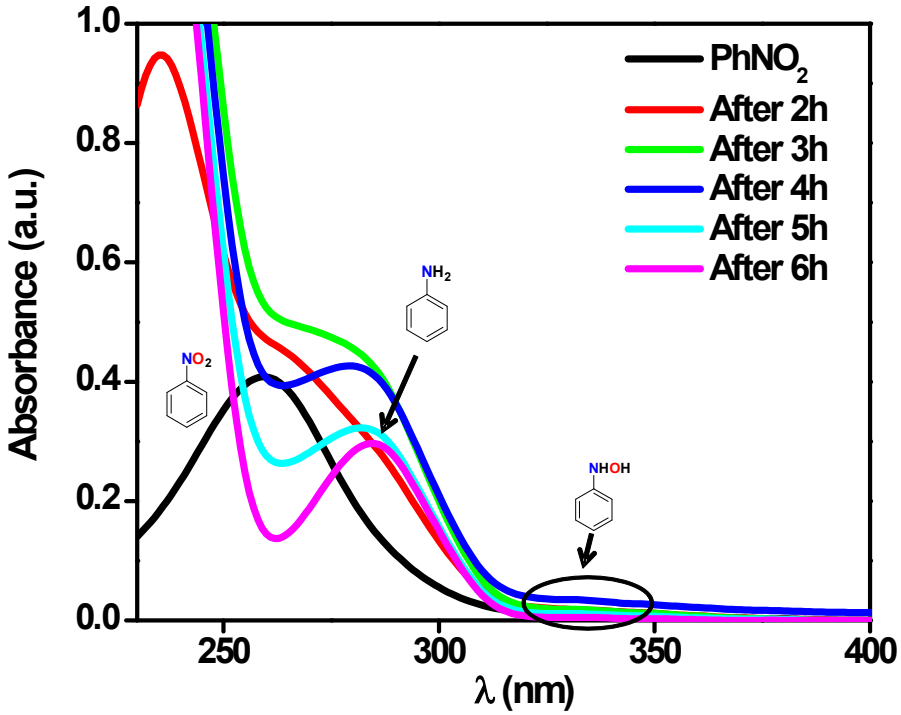

Figure S17. UV-vis spectra monitored at different time intervals during the reduction of nitrobenzene with hydrazine in MeOH using complex **1** as the catalyst.

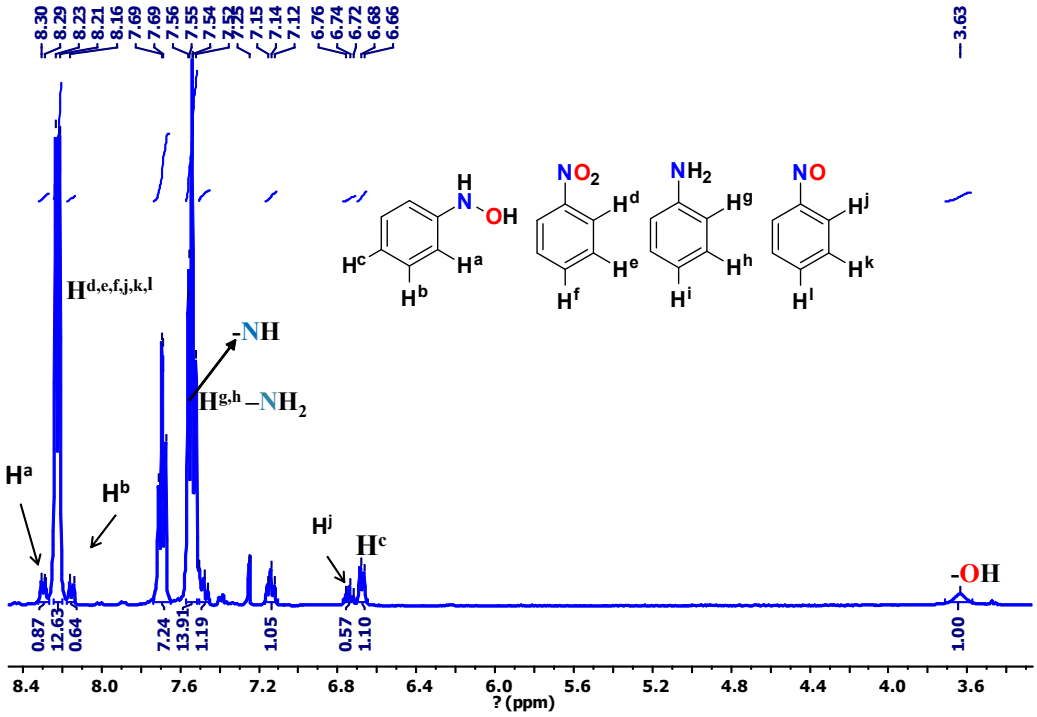

Figure S18. ^{1}H NMR spectrum (recorded in $CDCl_3$) of a reaction mixture during the reduction of nitrobenzene with hydrazine in MeOH using complex **1** as the catalyst.

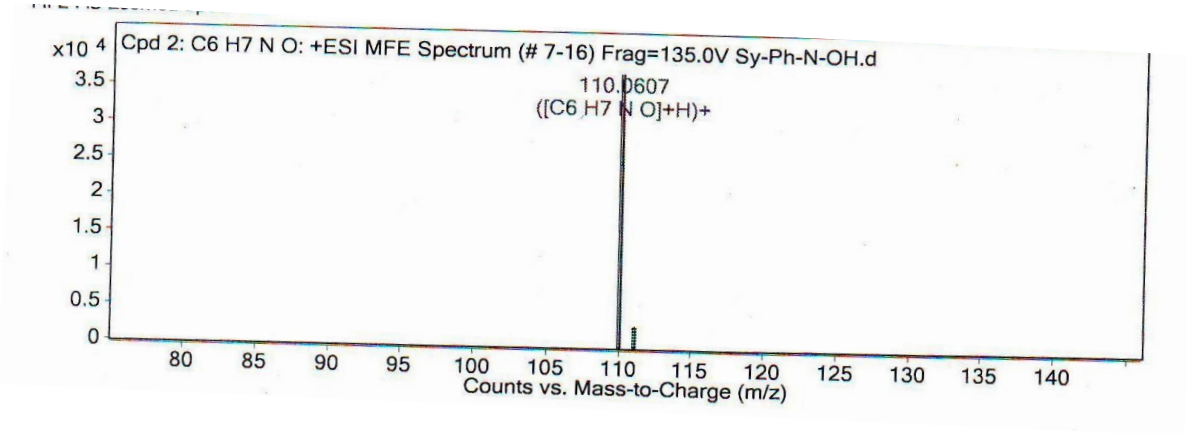

Figure S19. ^{1}H NMR spectrum (recorded in $CDCl_3$) of a reaction mixture displaying the formation of *N*-phenylhydroxylamine as one of the products during the reduction of nitrobenzene with hydrazine in MeOH using complex **1** as the catalyst.

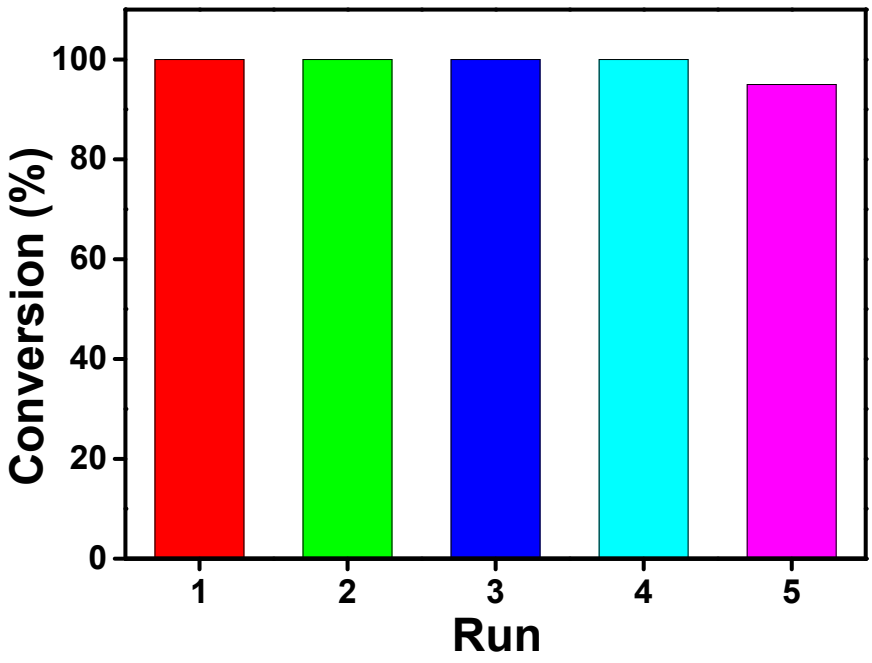

Figure S20. Recyclability experiments for the reduction of *para*-$CNPhNO_2$ with hydrazine in MeOH using complex **1** as a catalyst. In this experiment, a fixed amount of complex **1** (1-mol%) was taken in a reaction flask while fresh batches of *para*-$CNPhNO_2$ (1 equiv.) and hydrazine (2 equiv.) were added in five consecutive runs.

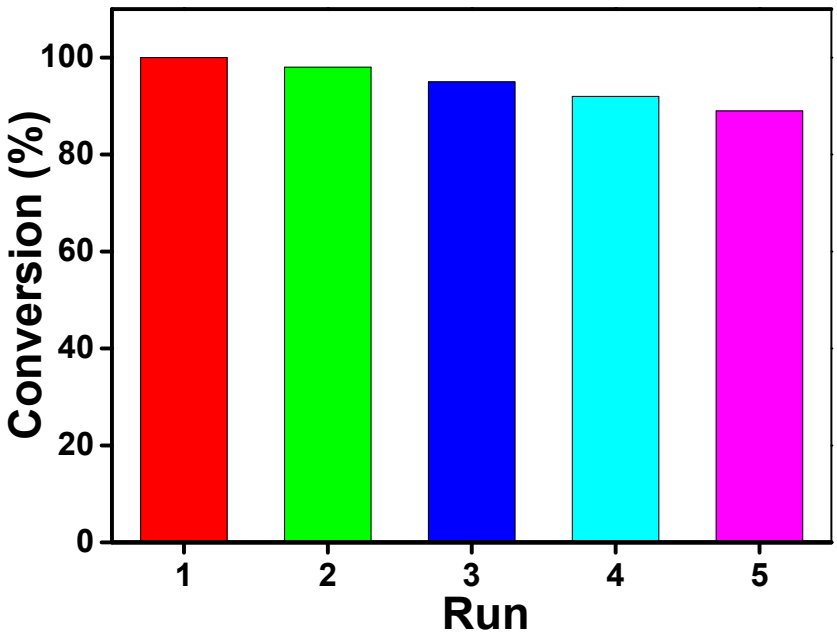

Figure S21. Recyclability experiments for the reduction of *para*-$CNPhNO_2$ with hydrazine in MeOH using complex **1** as a catalyst which was isolated at the end of every catalytic cycle (runs 1 – 5) and reused in the next cycle without any purification.

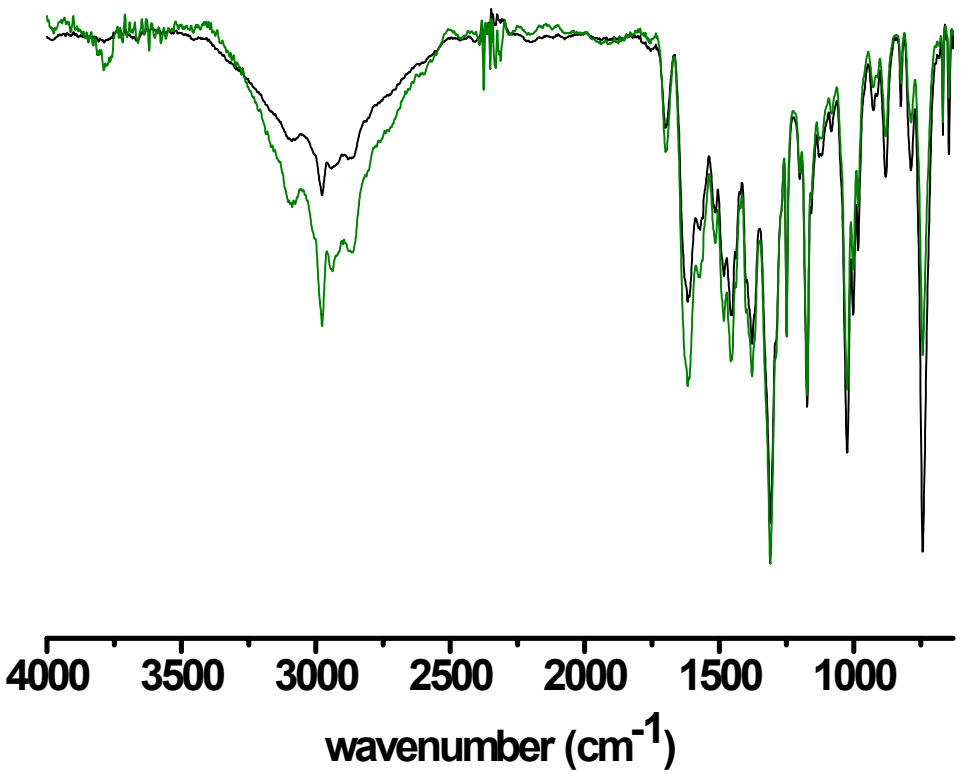

Figure S22. Comparative FTIR spectra of complex **1** before (green trace) and after (black trace) the catalysis.

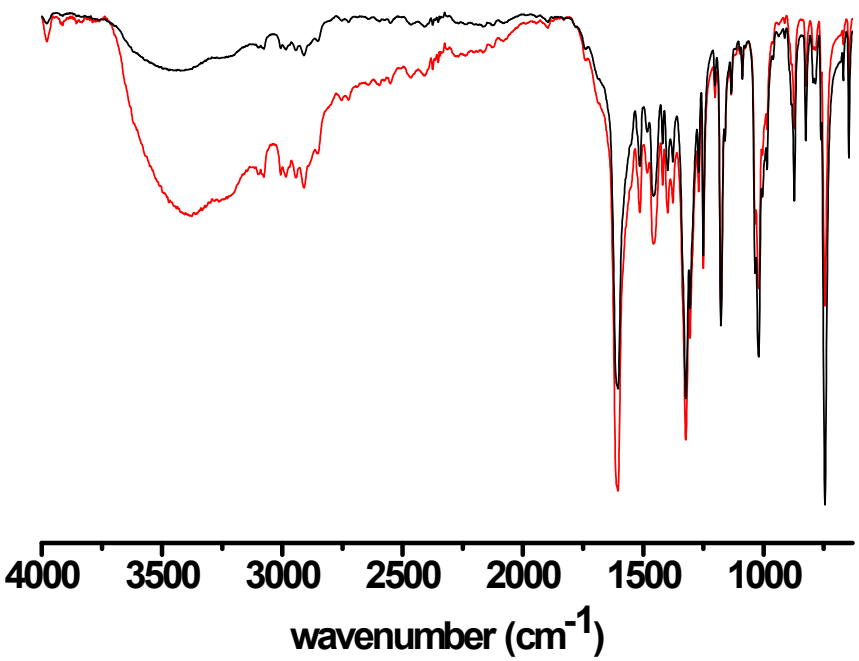

Figure S23. Comparative FTIR spectra of complex **2** before (red trace) and after (black trace) the catalysis.

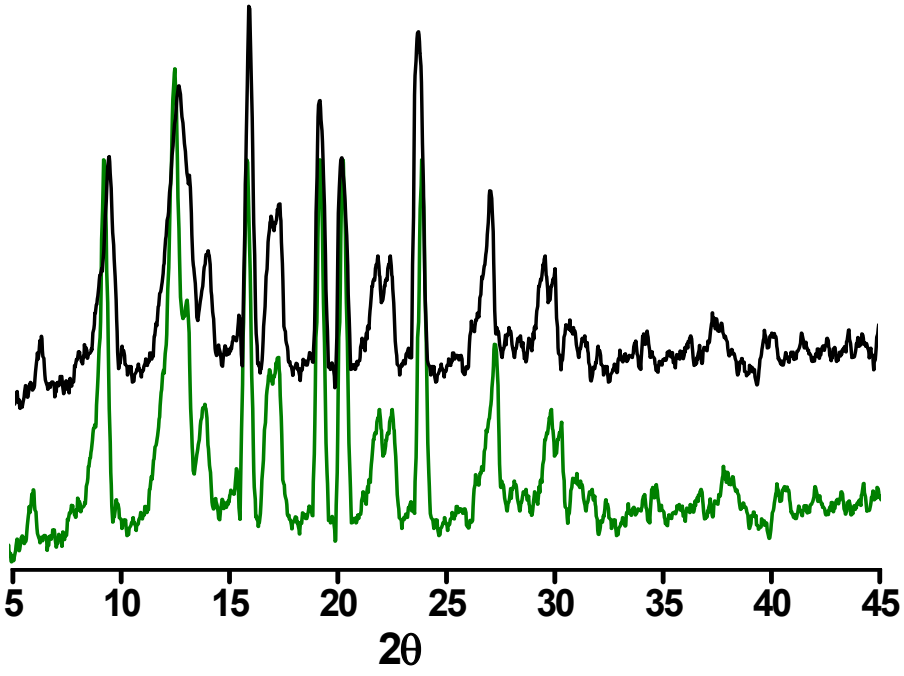

Figure S24. Comparative powder XRD patterns of as synthesized complex **1** (green trace) and the one measured after the catalysis (black trace).

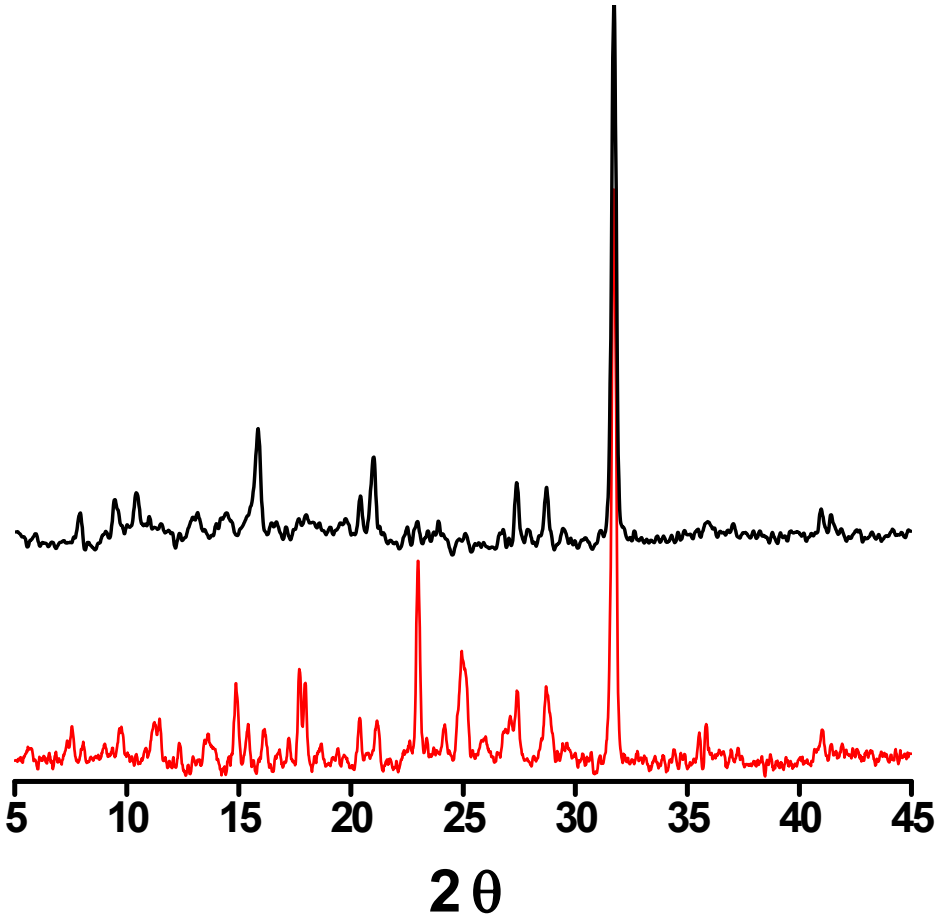

Figure S25. Comparative powder XRD patterns of as synthesized complex **2** (red trace) and the one measured after the catalysis (black trace).

Table S1. Crystallographic data collection and structure refinement parameters for complex **1**.

Empirical formula	$C_{24}H_{28}N_5O_2Cl_2Co$
Formula weight	548.34
Temperature	293(2) K
Wavelength	0.71073 Å
Crystal system	orthorhombic
Space group	$P\,2_1\,2_1\,2_1$
a	12.4118(9) Å
b	13.9055(16) Å
c	13.9670(16) Å
α	90°
β	90°
γ	90°
Volume	2410.6(4) $Å^3$
Z	4
Density (calculated)	1.511 Mg/m^3
Absorption coefficient	0.966 mm^{-1}
$F(000)$	1136
Crystal size	0.23 x 0.22 x 0.19 mm^3
Theta range for data collection	3.26 to 25.00°
Index ranges	$-14 \leq h \leq 14$, $-14 \leq k \leq 16$, $-16 \leq l \leq 14$
Reflections collected	9844
Independent reflections	4184 [R(int) = 0.0756]
Completeness to theta = 25.00°	98.9 %
Absorption correction	Multi-scan
Max. and min. transmission	0.8377 and 0.8084
Refinement method	Full-matrix least-squares on F^2
Data / restraints / parameters	4184 / 0 / 307
Goodness-of-fit on F^2	1.167
Final R indices [I>2sigma(I)][a, b]	$R_1 = 0.0835$, $wR_2 = 0.2028$
R indices (all data)	$R_1 = 0.0919$, $wR_2 = 0.2060$
Largest diff. peak and hole	1.540 and -0.848 $e.Å^{-3}$

[a] $R = \sum(\|Fo| - |Fc\|)/\sum|Fo|$; [b] $wR = \{\sum[w(F_o^2 - F_c^2)^2]/\sum[w(F_o^2)^2]\}^{1/2}$